

Tailoring a local acid-like microenvironment for efficient neutral hydrogen evolution

Received: 1 February 2023

Accepted: 6 July 2023

Published online: 14 July 2023

Check for updates

Xiaozhong Zheng¹, Xiaoyun Shi¹, Honghui Ning¹, Rui Yang¹, Bing Lu¹, Qian Luo¹, Shanjun Mao¹, Lingling Xi¹ & Yong Wang^{1,2}✉

Electrochemical hydrogen evolution reaction in neutral media is listed as the most difficult challenges of energy catalysis due to the sluggish kinetics. Herein, the Ir-H_xWO₃ catalyst is readily synthesized and exhibits enhanced performance for neutral hydrogen evolution reaction. H_xWO₃ support is functioned as proton sponge to create a local acid-like microenvironment around Ir metal sites by spontaneous injection of protons to WO₃, as evidenced by spectroscopy and electrochemical analysis. Rationalized revitalized lattice-hydrogen species located in the interface are coupled with H_{ad} atoms on metallic Ir surfaces via thermodynamically favorable Volmer-Tafel steps, and thereby a fast kinetics. Elaborated Ir-H_xWO₃ demonstrates acid-like activity with a low overpotential of 20 mV at 10 mA cm⁻² and low Tafel slope of 28 mV dec⁻¹, which are even comparable to those in acidic environment. The concept exemplified in this work offer the possibilities for tailoring local reaction microenvironment to regulate catalytic activity and pathway.

Sustainable electrocatalytic hydrogen evolution reaction (HER) using renewables powered, low-temperature water electrolyzers is promising for the deployment of the hydrogen economy for sustainable energy storage, transportation, and chemical production^{1–7}. It is well-established that this reaction starts with the Volmer step, which generates adsorbed hydrogen intermediates (H_{ad}) via electrochemical reduction of either hydronium ion (in an acidic medium) or water (in a neutral or alkaline medium). Subsequently, molecular hydrogen is produced by either a Tafel recombination step (H_{ad} + H_{ad} → * + H₂) or a charge-transfer Heyrovsky step (H_{ad} + H₂O + e⁻ → * + H₂ + OH⁻)^{8–13}. The kinetics of HER in neutral/alkaline medium is much sluggish than that in acidic environment because of the low concentration of protons. Consequently, even the state-of-the-art Pt-based catalyst, shows two to three orders of magnitude lower activity in neutral/alkaline media as compared to acidic media¹⁴. The kinetics of HER is strongly relevant to both the nature of electrode materials and the local reaction microenvironment in the vicinity of the catalytic sites at electrolyte–solid interface^{15–20}. To date, substantial progress has been made in promoting the kinetics of the electrode reactions by ameliorating the catalyst materials through various ways, such as introducing oxophilic

active elements^{21,22}, heterostructure modulating^{23,24}, strain engineering^{25,26}, nanoscopic confinement^{27,28}. Apparently, in most cases, these conventional strategies can only modulate their electronic states, adsorption capability of intermediates, and thereby catalytic properties in a gradual or mild way. However, these still cannot get rid of the pH-dependent kinetics of HER, leading to the inability to achieve big breakthroughs in the non-acidic electrolyte. Therefore, selecting a suitable system to create a local acid-like environment through multiple physicochemical effects to the maximum extent possible, will provide an alternative way to promote the electrocatalytic performance and guide the higher efficiency electrocatalyst design in non-acidic electrolyte, especially in more challenging neutral media.

As the prototypical example, the reversible and rapid hydrogen doping of WO₃ to form H_xWO₃ bronze was well reported via electrochemical electron–proton co-doping^{29–33}, in which H atoms are incorporated as W–OH species with Brønsted acidity and reducing some W⁶⁺ to W⁵⁺ along with charge rearrangement. Protonated H_xWO₃ could act as a proton sponge and electron reservoir to create an acid-like microenvironment in the electric double layer, thereby further affecting the reaction barriers and pathway^{34–36}. However, the strong

¹Advanced Materials and Catalysis Group, Center of Chemistry for Frontier Technologies, State Key Laboratory of Clean Energy Utilization, Institute of Catalysis, Department of Chemistry, Zhejiang University, 310028 Hangzhou, P. R. China. ²College of Chemistry and Molecular Engineering, Zhengzhou University, 450001 Zhengzhou, China. ✉e-mail: chemwy@zju.edu.cn

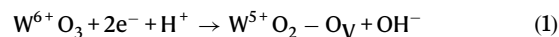
adsorption of hydrogen by basic oxygen centers and surface frustrated H–H coupling process severely hinder the local acidic species being rationally utilized. Enhancing electrochemical activation capability of H_xWO_3 via the addition of cocatalysts is of interest^{37–40}. Up to now, it still encounters many problems and challenges, for example, (1) the degree of local acidification of H_xWO_3 in neutral media has not been accurately quantified; (2) the synergistic catalysis between local acidic species and co-catalysts has not been fully understood; (3) the enhanced activity cannot be simply attributed to a single optimized catalytic site, and the origin of the activity deserves further investigation. In this work, typical tungsten oxide nanorods-arrays aligned on carbon fibers were deliberately selected as a host material. The WO_3 support experienced hydrogen insertion and Ir nanoparticles (NPs) electrodeposition processes to form hybridized Ir– H_xWO_3 . Experimental results and theoretical calculations deciphered that a high density of surface revitalized WO–H species enrich local proton concentration around Ir sites, and act as scavengers for H_{ad} on the metallic Ir to realize expedited hydrogen evolution rate, which is reflected in the fact that Ir– H_xWO_3 exhibits acid-like HER properties in neutral media.

Results and discussion

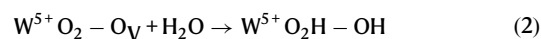
Hydrogen intercalation and storage of WO_3

The formation mechanism of H_xWO_3 bronze is dependent on the double injection of electrons and protons to the WO_3 nanorods grown on carbon fiber paper under cyclic voltammetry measurement (between 0 and -0.35 V vs. reversible hydrogen electrode, RHE) in 1.0 M PBS, as shown in Fig. 1a and Supplementary Fig. 1. Obviously, the color of the WO_3 electrode turns from yellow to dark blue (Fig. 1b and Supplementary Movie 1), which is a typical electrochromic process. Correspondingly, UV–vis diffuse reflectance spectra exhibit a prominent increase of absorption at a wavelength above 450 nm after

electrochemical hydrogenation (Fig. 1c), typically resulting from light absorption of the free electrons at oxygen vacancies (O_v) and the d-d transition of W^{5+} –OH (refs. 31,41). With increasing negative potentials, the electrons accumulated at the electrode/electrolyte interface, thus attracting the protons to reduce the lattice oxygen to produce O_v via the following reaction equation³¹, as reflected by a significant electron paramagnetic resonance (EPR) signal at $g = 2.003$ in Fig. 1d.



Surface active O_v is conducive to adsorbing and subsequently inducing dissociation of water molecules via transferring a proton to adjacent oxygen, thus forming terminal and bridging hydroxyls groups (W^{5+} –OH species) via the following reaction equation:



Undoubtedly, 1H solid-state nuclear magnetic resonance (NMR) spectroscopy (Fig. 1e) and X-ray photoelectron spectroscopy (XPS) results (Supplementary Fig. 2) confirm the above statements. Hydrogen intercalation fundamentally changes the interface properties of WO_3 . Electrochemical impedance spectroscopy (EIS, Fig. 1f) and Mott–Schottky measurement (M–S, Supplementary Fig. 3) are highly sensitive to detect the interface electron transfer and carrier density^{42,43}, respectively. An interface transfer resistance and corresponding dC^{-2}/dV significantly decreased after electrochemical protonation, which is ascribed to the high conductivity of W^{5+} –OH polaron states and high mobility of hydrogen on the WO_3 surface. Furthermore, protonation-driven semiconductor–metal conversion of WO_3 arises from a shift in electronic structure that is describable as a repositioning of the W d-bands in Fig. 1g.

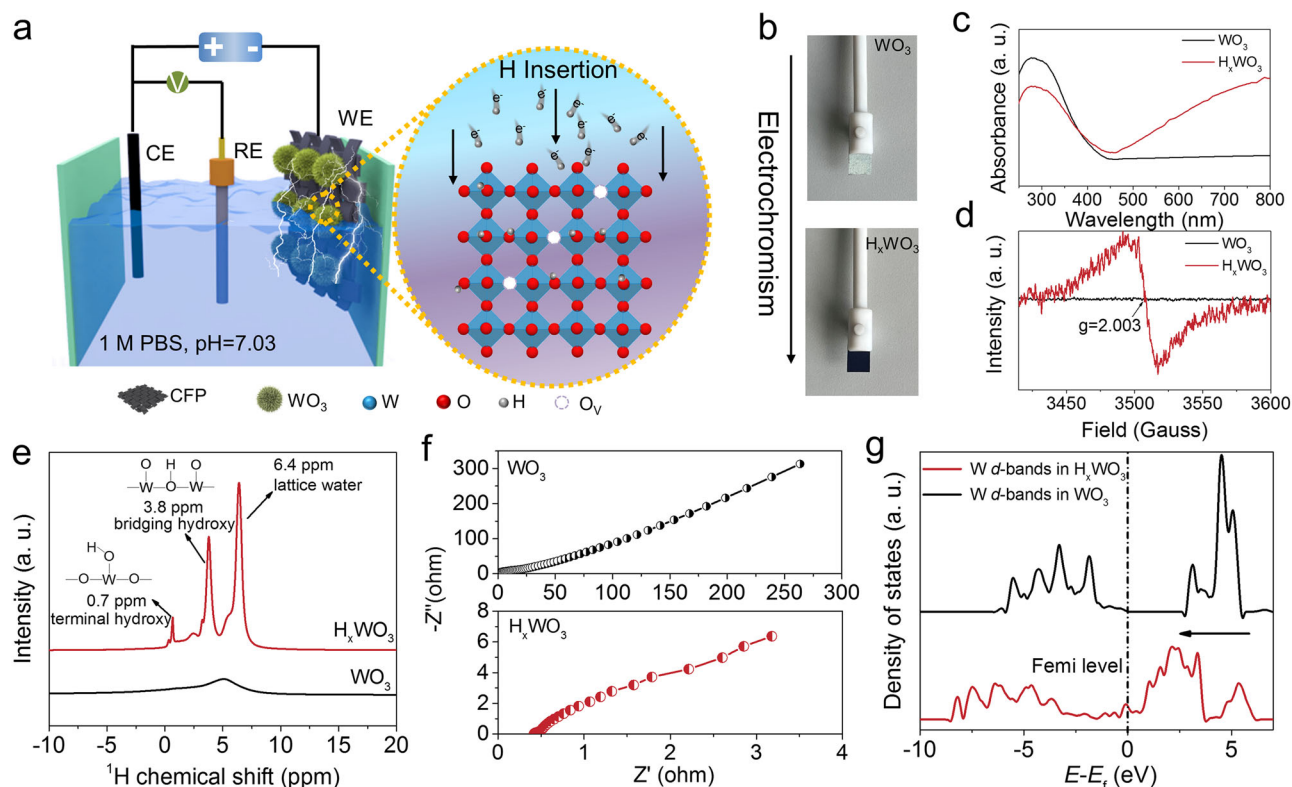


Fig. 1 | Hydrogen intercalation of WO_3 . **a** Schematic illustration of the hydrogen intercalation process of WO_3 to form H_xWO_3 . **b** Digital pictures of the WO_3 working electrode before and after electrochemical hydrogenation. **c** UV–vis diffuse reflectance spectra of WO_3 and H_xWO_3 . **d** EPR signal of oxygen vacancies. **e** 1H NMR

spectra of WO_3 and H_xWO_3 . **f** EIS Nyquist plots of different electrocatalysts measured at open circuit potential from 10 kHz to 0.01 Hz. **g** The pDOS curves of W d-bands of WO_3 and H_xWO_3 .

Local pH measurements and catalytic behaviors of H_xWO_3

We used the rotating ring-disk electrode (RRDE) technique^{19,44,45} to quantitatively detect local pH on the H_xWO_3 cathode surfaces at different applied potentials in neutral 1.0 M PBS solution (bulk pH is 7.03), along with classical carbon support for comparison (Supplementary Fig. 4–6, details see Methods). On the basis of RRDE detecting method, we found that the pH of the H_xWO_3 surface varies from 6.27 to 3.53 as potential decreases from 0.1 to $-0.4 V_{RHE}$, which undoubtedly confirms that H_xWO_3 acts as proton sponge to form a local acid-like microenvironment on the electrode surface (Fig. 2a, b). In sharp contrast, the pH of carbon cathode surface is maintained at ~ 7 in the range of 0.1 to $-0.4 V_{RHE}$ (Fig. 2b). As the potential continued to shift negatively, the pH of H_xWO_3 and carbon support surfaces gradually increases and approaches 8.32 and 8.0 at $-0.7 V_{RHE}$, respectively, due to the consumption of the local hydrogen species. Astonishingly, when the bias ($-0.7 V_{RHE}$) is removed, the surface of H_xWO_3 and carbon cathodes turn back to steady acidic (pH = 3.73) and neutral (pH = 7.12) states, respectively (Fig. 2c). We then move on to investigate the catalytic behaviors of H_xWO_3 in neutral media. Counterintuitively, despite the construction of a unique proton-rich microenvironment, the H_xWO_3 grown on CFP material still provides a high overpotential of 548 mV at 10 mA cm^{-2} (Fig. 2d). Following the insertion of hydrogen atoms, H-H coupling must occur to form molecular H_2 . This can take place through surface-mediated (Tafel step) or water-mediated (Heyrovsky step) routes⁸. In the surface-mediated mechanism, it is hard for two surface hydrogen atoms of H_xWO_3 to proceed H-H coupling because active hydrides are separated by relatively long distances (Supplementary Fig. 7), which is further reflected by high Tafel barrier (0.82 eV in Fig. 2f). In the water-mediated mechanism, surface hydrogen atoms form H_2 by reacting with water of the electrolyte. The analysis of the Tafel slope for H_xWO_3 (Fig. 1e) reveals that it obeys the water-mediated mechanism, but requires a high overpotential ($>500 \text{ mV}$) to drive it. As shown by density functional theory (DFT) calculations in Fig. 2f and Supplementary Fig. 8, the poor catalytic activity of H_xWO_3 catalyst is

well explained by the fact that surface water-mediated H-H transfer predominates in the early stage of HER and water-mediated H-H coupling occurs only when the overpotential is largely increased. The weak electrochemical activation capability of H_xWO_3 severely prevents its hydrides from being properly utilized⁴⁶. To tackle this problem, the construction of H_xWO_3 with metal-based materials is considered as a promising design strategy in the following two aspects: (1) interfacial polarization electric field generated by metal and H_xWO_3 to activate lattice-hydrogen species; (2) providing additional active sites to promote interfacial synergistic effects between them.

Synthesis and characterization of catalysts

Based on the above assumptions, Ir- H_xWO_3 hybrid electrocatalyst was intentionally manufactured similar to that of H_xWO_3 except for adding 0.2 g L^{-1} $IrCl_3$ to 1.0 M PBS solution. Ir^{3+} precursors are progressively reduced to metallic Ir nanoparticles (NPs) under applied negative bias, as revealed by the HER activity enhancement increases with cycles, eventually leveling off after 500 cycles in Supplementary Fig. 9. Ir content in Ir- H_xWO_3 hybrid electrocatalyst is 2.8 wt% (or $47 \mu\text{g cm}^{-2}$ when normalized to geometric area of electrode) determined by inductively coupled plasma-optical emission spectrometry (ICP-OES, Supplementary Table 1). X-ray diffraction (XRD) patterns in Fig. 3a disclose that as-prepared WO_3 , H_xWO_3 , and Ir- H_xWO_3 electrocatalysts exhibit clear diffraction peaks of hexagonal WO_3 (JCPDS No. 85-2460), but no diffraction peaks related to H_xWO_3 . Notably, the characteristic diffraction peaks of WO_3 in H_xWO_3 and Ir- H_xWO_3 catalysts are shifted toward a low-angle direction (Supplementary Fig. 10), probably ascribing to oxygen defect-induced lattice extension⁴⁷. Meanwhile, for Ir- H_xWO_3 , the signals of Ir NPs are not detected, possibly due to their small sizes and low content. As revealed in Supplementary Fig. 11, 12 and Fig. 13a–c, after electrochemical protonation, the scanning electron microscopy (SEM) and transmission electron microscopy (TEM) images display that H_xWO_3 and Ir- H_xWO_3 samples inherit the original WO_3 nanorods-like morphology. Comparatively, the TEM images

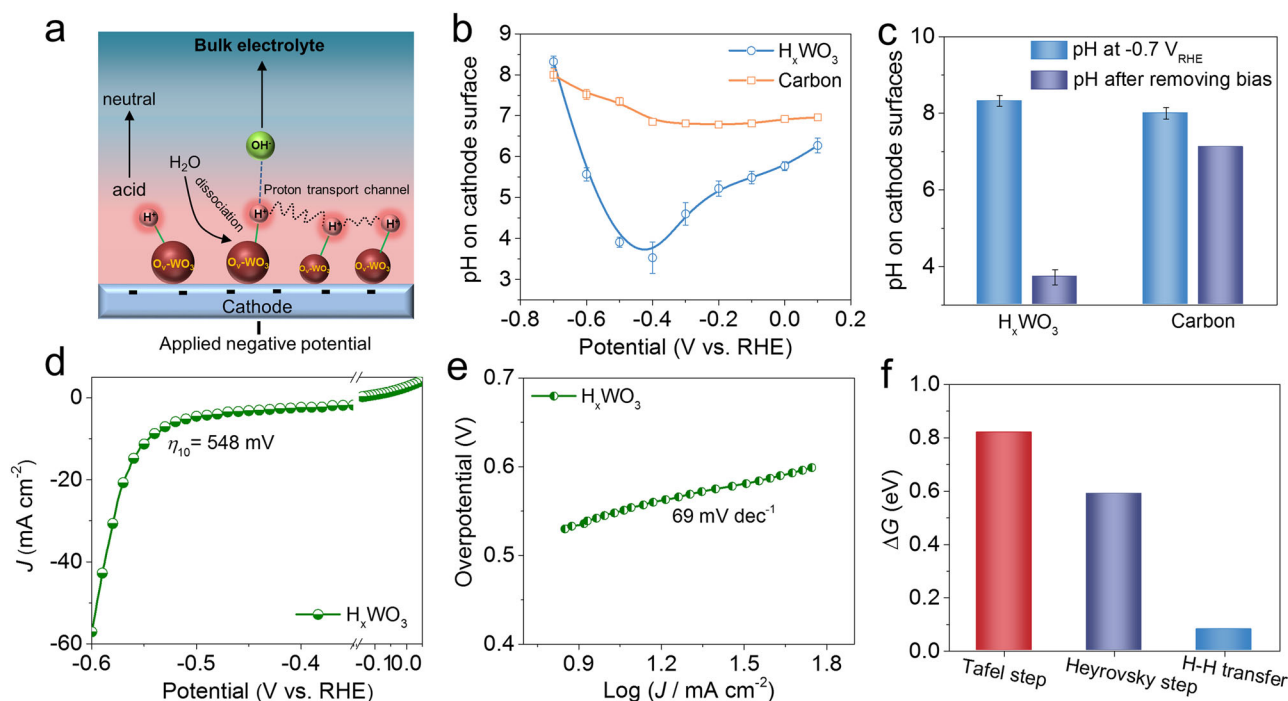


Fig. 2 | Local pH measurements and catalytic behaviors of H_xWO_3 . **a** Schematic diagram of local acid-like microenvironment generation on H_xWO_3 cathode. **b** Measured pH values on H_xWO_3 and carbon cathode surfaces at different potentials, respectively. **c** The pH on H_xWO_3 and carbon cathode surfaces before and

after removing bias ($-0.7 V_{RHE}$). **d** HER polarization curves of H_xWO_3 grown on CFP with 95% iR compensation and **(e)** corresponding Tafel plots. **f** Free energy barriers of H-H coupling and H-H transfer in H_xWO_3 . Note: error bars represent the standard deviation of three independent measurements.

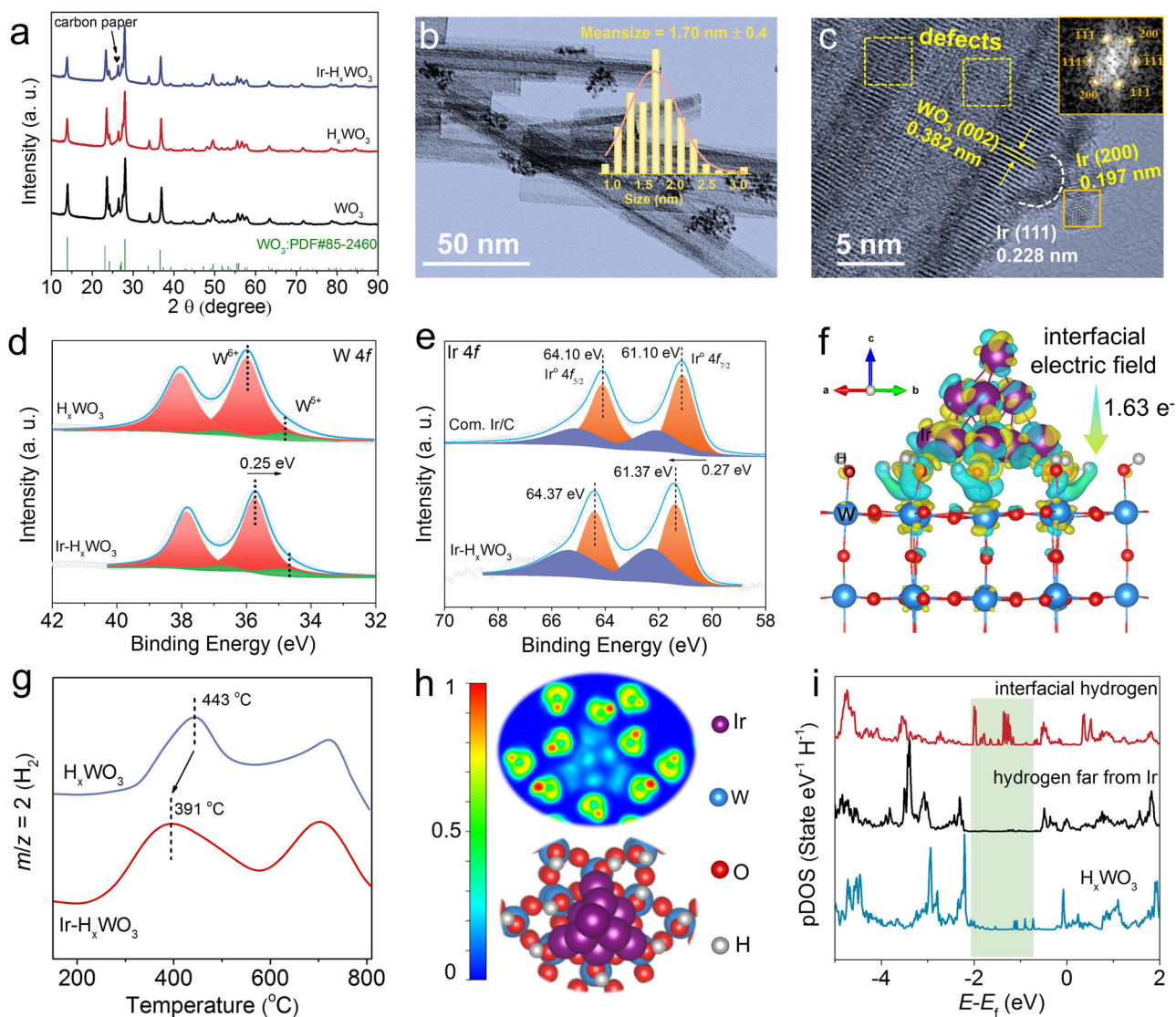


Fig. 3 | Structural characteristics of catalysts. a XRD patterns of as-obtained WO_3 , H_xWO_3 and $\text{Ir-H}_x\text{WO}_3$. **b** Typical TEM image of $\text{Ir-H}_x\text{WO}_3$, the inset in **(b)** shows the Ir NPs size distribution pattern. **c** HAADF-STEM images of $\text{Ir-H}_x\text{WO}_3$, with the inset in **(c)** giving the fast Fourier transform of the corresponding Ir NP. **d** High-resolution W 4f spectra of $\text{Ir-H}_x\text{WO}_3$ and H_xWO_3 . **e** High-resolution Ir 4f spectra of $\text{Ir-H}_x\text{WO}_3$ and commercial Ir/C. **f** The side views of charge density difference in the

interface of Ir_{10} clusters supported on H_xWO_3 . The cyan region reflects an electron-deficient state while the yellow region reflects an electron-rich area, with an iso-value of $0.004 e^-/\text{\AA}^3$. **g** Representative TPD-MS thermal desorption profiles for $\text{Ir-H}_x\text{WO}_3$ and H_xWO_3 and the main desorbed specie detected is H_2 with $m/e = 2$. **h** Electron localization function evaluations of $\text{Ir}_{10}\text{-H}_x\text{WO}_3$. **i** The pDOS curves of 1s orbitals of different hydrogen atoms in $\text{Ir}_{10}\text{-H}_x\text{WO}_3$ and pure H_xWO_3 .

(Fig. 3b and Supplementary Fig. 13d–f) of $\text{Ir-H}_x\text{WO}_3$ demonstrate that Ir NPs with mean size of ~ 1.7 nm are embedded on H_xWO_3 nanorods. Corresponding EDS elemental mapping images and line-scan profiles (Supplementary Fig. 13g–k) further verify the successful loading of Ir. The Ir NPs exhibit clear lattice fringes with interplanar distances of 1.97 and 2.28 Å, corresponding to the [200] and [111] crystal planes of the [011] face-centered cubic Ir, respectively, further evidenced by the fast Fourier transform (FFT) pattern (Fig. 3c). Meanwhile, the disordered structures identified by deformed and blurred lattice fringes belonging to [002] plane of WO_3 are found in $\text{Ir-H}_x\text{WO}_3$ (Fig. 3c), which is ascribed to a good deal of surface defects induced by hydrogen intercalation during electrochemical activation⁴⁸. Subsequently, XPS was carried out to further analyze the atomic structure and surface valence of catalysts. The typical W 4f spectra of H_xWO_3 and $\text{Ir-H}_x\text{WO}_3$ indicate the coexistence of W^{6+} and W^{5+} (Fig. 3d)³⁰. Compared with those of H_xWO_3 , W 4f binding energies of the $\text{Ir-H}_x\text{WO}_3$ show a significant redshift of 0.24 eV. The O 1s split-peak fitting results (Supplementary Fig. 14) reveal that lattice oxygen, surface hydroxyl, and adsorbed

water species are detected on the surface of H_xWO_3 and $\text{Ir-H}_x\text{WO}_3$ samples. As expected, after Ir NPs loading, the O 1s spectrum of $\text{Ir-H}_x\text{WO}_3$ moves toward lower binding energies. Figure 3e demonstrates the comparison of Ir 4f XPS spectra between commercial Ir/C and $\text{Ir-H}_x\text{WO}_3$. It is noticeable that the binding energy of Ir for $\text{Ir-H}_x\text{WO}_3$ is positively shifted by 0.27 eV up to 61.37 eV ($\text{Ir}^0 4f_{7/2}$) and 64.37 eV ($\text{Ir}^0 4f_{5/2}$). These results manifested the strong electronic interaction between Ir NPs and H_xWO_3 support. Further, the charge density difference diagram of the interface between Ir NPs and H_xWO_3 (Fig. 3f) reveals a charge transfer of $1.63 e^-$ from the Ir atom to H_xWO_3 through interfacial Ir–O–W bond, confirming the XPS results. In addition, the planar average potential plots along the Z-direction (Supplementary Fig. 15) confirm the interfacial built-in electric fields in $\text{Ir-H}_x\text{WO}_3$.

Undoubtedly, the strong electric field effect at the interface between Ir NPs and H_xWO_3 will affect the lattice-hydrogen species in H_xWO_3 support. The ^1H NMR spectra (Supplementary Fig. 16) confirm the signals of $\text{Ir-H}_x\text{WO}_3$ broadens and moves toward higher fields (1.1

and 4.0 ppm) compared to those of H_xWO_3 (0.7 and 3.8 ppm), which indisputably reveal that the acid strength of Ir- H_xWO_3 material is stronger than that of H_xWO_3 (ref. 49). Stronger acid strength also means easier detachment of protons. To prove this statement, temperature-programmed desorption (TPD) coupled with mass spectrometry ($m/z = 2$, H_2) was performed to investigate the desorption behavior of lattice-hydrogen species over H_xWO_3 and Ir- H_xWO_3 . As demonstrated in Fig. 3g, the TPD profiles of Ir- H_xWO_3 and H_xWO_3 are characterized by two typical peaks, assigned to the recombination of surface and bulk hydroxyl groups producing H_2 (ref. 50), respectively. It is worth noting that the introduction of Ir accelerates the desorption of lattice-hydrogen species in the H_xWO_3 support, as revealed in shifting towards low temperature of Ir- H_xWO_3 TPD pattern compared to pure H_xWO_3 . We next considered the chemical reasons for why Ir metal profoundly changes the behavior of hydrogen desorption over H_xWO_3 surfaces. The contour map of electron localization function (ELF) for Ir- H_xWO_3 is shown in Fig. 3h, projected over the [001] plane to analyze the electron localization and bond polarity characters⁵¹. The addition of Ir in the H_xWO_3 structure leads to the localized electron density redistribution of WO-H species adjacent to Ir NPs (denoted as interfacial hydrogen species) and the formation of more polar O-H bonds. Contrariwise, O-H bonds far from Ir metal exhibit a considerably covalent character. Bader charge analysis was conducted to quantitatively study the charge distribution. In Supplementary Fig. 17, the average Bader charges value of interfacial hydrogen atoms is 0.341 e^- , which is significantly lower than that of the hydrogen atoms far away from Ir (0.365 e^-) and pure H_xWO_3 (0.361 e^-). Further extracting the projected density of states (pDOS) curves of different chemical states of lattice-hydrogen species, as shown in Fig. 3i, it is well noted that interfacial-hydrogen species possess a higher electronic state near the Fermi level compared to pure H_xWO_3 and hydrogen species far from Ir metal, indicating that metallic Ir revitalizes the lattice-hydrogen species and enabling it possible to participate in the HER process.

Electrocatalytic HER performances

Encouraged by a local activated acid-like microenvironment created around Ir NPs in Ir- H_xWO_3 , it is expected to be able to substantially boost HER activity in non-acidic environments. Thus, the electrocatalytic HER activity of Ir- H_xWO_3 , commercial 20 wt% Pt/C and 10 wt% Ir/C catalysts were tested in a conventional three-electrode electrochemical cell with H_2 -saturated 1.0 M PBS as electrolyte (Supplementary Fig. 18), along with acidic HER evaluation in 0.5 M H_2SO_4 for comparison. The catalytic activity was obtained from iR-compensated linear sweep voltammetry (LSV) curves, and different levels of iR compensation were considered and presented in Supplementary Fig. 19. To avoid potentiostat oscillation and overcorrected results⁵², automatically 95% iR compensation was adopted in this electrochemical test. As expected, in Fig. 4a–c, the HER activity and kinetics of Ir- H_xWO_3 under neutral conditions are similar to those in acidic media. Specifically, at an overpotential of 150 mV, Ir- H_xWO_3 can deliver 256 mA cm^{-2} in neutral media, but it only increases to 277 mA cm^{-2} under acidic media. The close Tafel slope values (neutral: 28 mV dec^{-1} ; acidic: 25 mV dec^{-1}) indicate a similar hydrogen evolution pathway (Tafel step: $H_{ad} + H_{ad} \rightarrow * + H_2$). However, striking performance discrepancy is observed in well-known Pt/C and Ir/C electrocatalysts in different electrolytes. In acidic media, the current density of Pt/C and Ir/C is 2.62 and 6.18 times higher than those in neutral medium at 150 mV overpotential. The significantly reduced Tafel slopes manifests that HER catalytic kinetics is strongly related to the proton concentration. These results corroborate that for conventional carbon-supported metal catalysts exhibit highly pH-dependent catalytic activity, while H_xWO_3 plays as proton sponge to create acid-like microenvironment around metal catalysts to obtain thermodynamically favorable catalytic activity and accelerated reaction kinetics in a proton-deficient neutral media. It is noteworthy that the

Ir- H_xWO_3 ($\eta_{10} = 20$ mV; Tafel slope: 28 mV dec^{-1}) is among the best HER electrocatalysts reported in the neutral medium (Fig. 4d and Supplementary Table 2). Accelerated HER kinetic of Ir- H_xWO_3 is also reflected by the smaller charge-transfer resistance (the width of the semicircle, 2.5 Ω , Fig. 4e). To further identify its high intrinsic HER activity, being normalized to the per milligram noble-metal loading, Ir- H_xWO_3 (5.46 A mg_{Ir}^{-1}) exhibits 4.3 and 13.3 times higher mass activity than those of Pt/C (1.27 A mg_{Pt}^{-1}) and Ir/C (0.41 A mg_{Ir}^{-1}) at an overpotential of 150 mV (Fig. 4f).

High-speed imaging experiments prove that the superhydrophilic structure (surface W-OH group) of Ir- H_xWO_3 better suppresses bubble coalescence and enhances bubble release compared to commercial Pt/C counterpart (Fig. 4g and Supplementary Movie 2–3), so Ir- H_xWO_3 was proposed to have better catalytic performance for water splitting, especially at high current densities. Additionally, we performed the stability test for fully assessing the catalyst via the accelerating degradation technique (ADT) and potential-constant electrolysis. Supplementary Fig. 20 shows the polarization curve of Ir- H_xWO_3 manifests negligible shift after 10,000 ADT cycling tests. The long-term durability testing on the Ir- H_xWO_3 catalyst by a static chronopotentiometry test (at 10 mA cm^{-2} in Fig. 4h) even represents a relatively stable horizontal line with an overpotential increase of only 14 mV over 100 operating hours, while Pt/C exhibits a clipping activity decay within a few hours, demonstrating the good activity retention of Ir- H_xWO_3 . However, it is still a challenge to develop efficient catalysts working at large current density for neutral water splitting. Amazingly, Ir- H_xWO_3 catalyst maintains operation stability at a large current density of 500 mA cm^{-2} over 40 h, outperforming most of the recently reported landmark catalysts (Supplementary Table 2). Both the structure and composition of Ir- H_xWO_3 remain unchanged before and after the HER stability test as examined by XRD, SEM, HRTEM and ICP-OES (Supplementary Fig. 21 and Table 2). For practical application, natural seawater splitting performance is also evaluated. As expected, in Supplementary Fig. 22, Ir- H_xWO_3 exhibits good HER performance in natural seawater, requiring an overpotential of 150 mV to produce 10 mA cm^{-2} of catalytic current density. This is lower than that of Pt/C (295 mV) and other state-of-art catalysts (Supplementary Table 3). In summary, the efficient Ir- H_xWO_3 catalyst under neutral/near-neutral conditions is expected to be applied for next-generation water-splitting technologies.

Exploration of catalytic mechanisms

To gain more insights into the original active sites of electrocatalysts, the operando electrochemical Raman spectra were then recorded to investigate the neutral HER behavior at the Ir- H_xWO_3 and H_xWO_3 surfaces (Supplementary Fig. 23). For H_xWO_3 sample, as indicated in Fig. 5a, b, the intensity of typical peaks at 762 cm^{-1} , 714 cm^{-1} (stretching vibrations of O-W-O skeleton) and 926 cm^{-1} (stretching vibrations of terminal W=O bond) sharply weaken from open circuit potential (OCP) to $-0.1 V_{RHE}$. Further decreasing potential (-0.15 to $-0.3 V_{RHE}$), all of these characteristic peaks disappear, accompanied by the increasing intensity of the ~ 1580 and 2715 cm^{-1} band from the bending and stretching vibration modes of WO-H species^{53–55}. This observation confirms that hydrogen insertion occurs in WO_3 in response to the cathodic voltage, where the H atoms are incorporated into the Brønsted acidic W^{5+} -OH groups, and the hydrogen storage saturates after the potential reaches $-0.15 V_{RHE}$. However, the lack of H-H coupling sites and weak electrochemical activation prevent the surface hydride from being effective as H_2 molecular from the surface, which is reflected by its poor catalytic activity. Additionally, the variation trends of the two broad bands at 3249 and 3407 cm^{-1} (Fig. 5a, c), assignable to tetrahedrally and trihedrally coordinated water at the interface^{56,57}, suggest that the process of hydrogen incorporation is closely related to the activation of interfacial water. In stark contrast, with regard to Ir-modified H_xWO_3 electrocatalyst (Fig. 5d, e), the Raman signals of

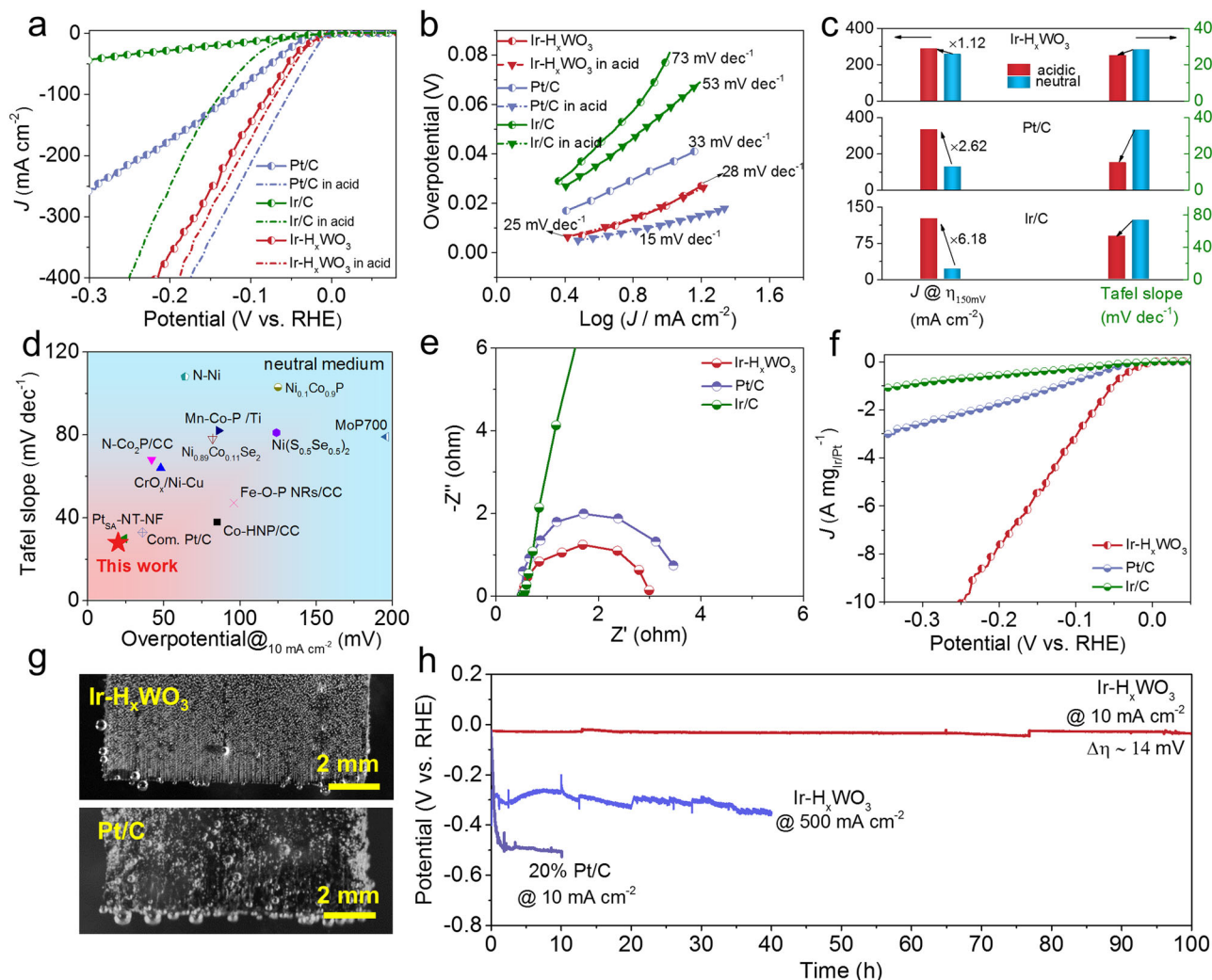


Fig. 4 | Electrochemical HER performances. **a** HER polarization curves of different electrocatalysts in 1.0 M PBS and 0.5 M H₂SO₄ at 2 mV s⁻¹ scan rate. **b** Tafel plots obtained from the polarization curves. **c** Comparison of current density (@η_{150 mV}) and Tafel slopes of different electrocatalysts in acidic and neutral media. **d** Comparison of neutral HER activity between Ir-H_xWO₃ and recently reported electrocatalysts. **e** EIS Nyquist plots of different electrocatalysts measured at -0.03

V_{RHE} from 10 kHz to 0.01 Hz in 1.0 M PBS. **f** Mass activity of electrocatalysts. **g** The H₂ bubbles desorption behaviors of Ir-H_xWO₃ and commercial Pt/C at 100 mA cm⁻². **h** Chronopotentiometry tests of Ir-H_xWO₃ (@10 and 500 mA cm⁻²) and commercial 20% Pt/C (@10 mA cm⁻²) in 1.0 M PBS. All electrochemical data were corrected for 95% iR drop.

W-O-W, W=O and WO-H progressively weaken over the whole potential range (OCP to -0.3 V_{RHE}), which further illustrates that the Ir-H_xWO₃ depleted surface WO-H species during HER process to alleviate deep-hydrogenation of H_xWO₃ supports. Moreover, compared with H_xWO₃, the apparent increased intensity of O-H stretching vibrations signals at 3249 and 3407 cm⁻¹ and the appearance of H-O-H bending vibration bands at 1650 cm⁻¹ are detected⁵⁷ (Fig. 5d, f), indicating that Ir NPs enhance the adsorption of interfacial water molecules. As subsequent HER going on, the activity of H₂O continued to decrease, verifying that Ir serves as the site of water dissociation. Based on the results of operando electrochemical Raman spectra, it is plausible that there may be possible synergistic catalysis between Ir and lattice-hydrogen species derived from H_xWO₃.

To verify this hypothesis, first of all, selectively poisoning experiments were conducted. Based on the well-established Li⁺-ion-exchange method³⁵ (WO-H + Li⁺ → WO-Li + H⁺), Ir-H_xWO₃ electrocatalyst was immersed in 0.5 M LiNO₃ solution for 12 h to completely realize H⁺-Li⁺ exchange. As shown in Fig. 6a, after Li⁺ poisoning, the striking activity decay of Ir-H_xWO₃ is observed, highlighting the importance of the local acidified environment for HER activity. The

same process was performed on Pt/C and H_xWO₃ support in Supplementary Fig. 24 for comparison to confirm Li⁺ selectively poisons the WO-H species and excludes its effect on the metal sites. In addition, it is well known that metal catalytic sites are very sensitive and reactive to SCN⁻, which can poison metal-centered catalytic sites by coordinating with metallic species strongly⁵⁸. The HER polarization plots of Ir-H_xWO₃ show the drastic negative shifts of potentials after the introduction of 20 mM SCN⁻ ions into the electrolyte (Fig. 6a). For comparison, after SCN⁻ treatments for Pt/C and H_xWO₃ support in Supplementary Fig. 25, an obvious activity reduction of Pt/C is detected and has no effect on H_xWO₃ support. Then, the Tafel slopes of Ir-H_xWO₃ catalyst before and after Li⁺ or SCN⁻ poisoning are compared to analyze the change of the catalytic reaction pathway. As shown in Fig. 6b and Supplementary Fig. 26, after WO-H replaced by WO-Li, the value of Tafel slope of catalyst increases from 28 to 89 mV dec⁻¹, manifesting that the rate-determining step (RDS) of the reaction changes from Tafel (H_{ad} + H_{ad} → * + H₂) to Heyrovsky step (H_{ad} + H₂O + e⁻ → * + H₂ + OH⁻)¹² and elucidating that the presence of lattice-hydrogen alters the catalytic mechanism. Furthermore, after poisoning the metal sites, the RDS transforms into Volmer step (158 mV dec⁻¹,

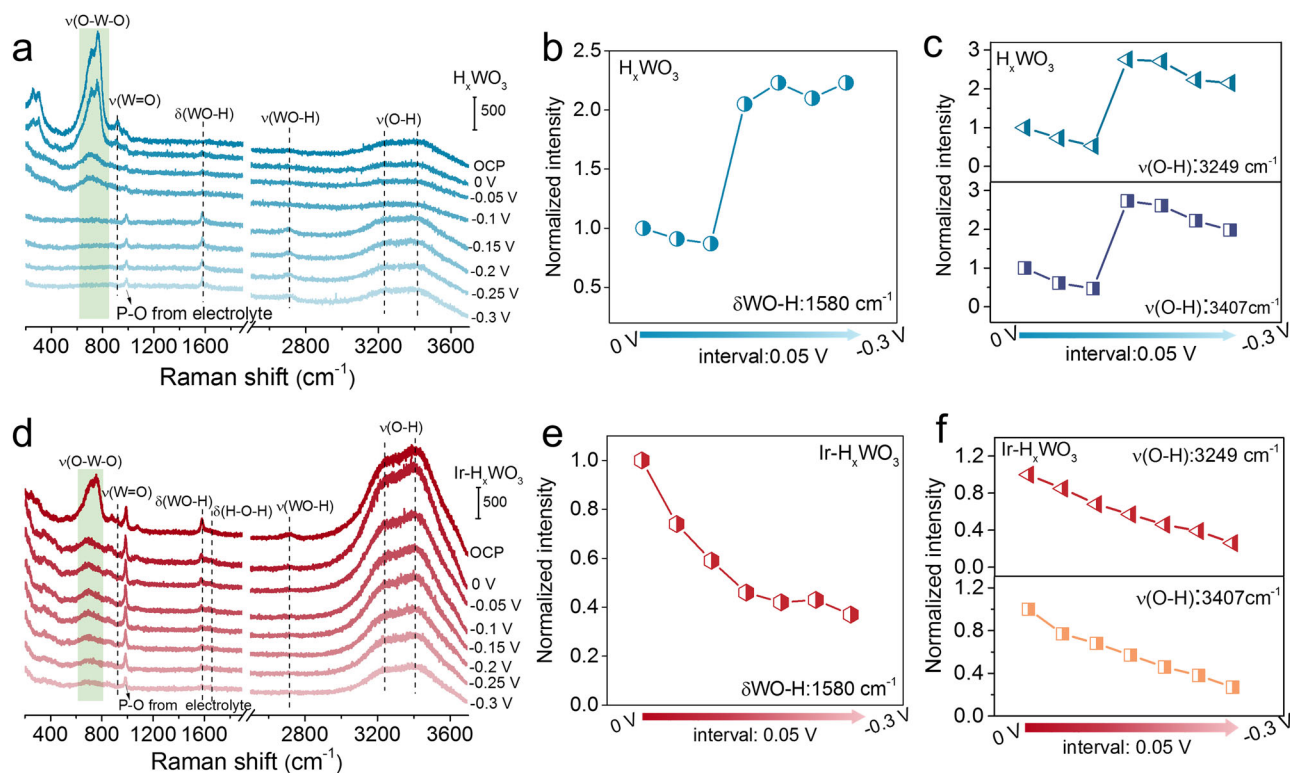


Fig. 5 | Operando electrochemical Raman measurements. **a** Operando electrochemical Raman spectra of H_xWO_3 from OCP to $-0.3 V_{RHE}$ and corresponding normalized intensity of WO-H (**b**) and O-H (**c**) signals under different HER

potentials. **d** Operando electrochemical Raman spectra of $Ir-H_xWO_3$ from OCP to $-0.3 V_{RHE}$ and corresponding normalized intensity of WO-H (**e**) and O-H (**f**) signals under different HER potentials.

$*H_2O + e^- \rightarrow *H + OH^-$)¹², significantly unveiling that Ir metal site is the response for the water dissociation, which is in line with the results of operando Raman spectra.

Further depicting the rate-limiting step, kinetic isotope effect (KIE) experiments were performed. The LSV curves and corresponding KIE values (J_{H_2O}/J_{D_2O} at $-0.1 V_{RHE}$) are recorded from $Ir-H_xWO_3$ in 1.0 M PBS aqueous electrolyte and 1.0 M PBS D_2O electrolyte (Fig. 6c, d). Interestingly, the LSV plots of $Ir-H_xWO_3$ demonstrate the negative shifts of potentials after several HER cycles and eventually stabilize after 7th LSV scan. These results reveal that the initial KIE effect (2.57) is possibly derived from the O-D bond activation/dissociation of deuterium water, and then surface active WO-H species are gradually replaced by WO-D, resulting in worse hydrogen transfer kinetics⁵⁹, which can be explained by the presence of an obvious induction period and corresponding increased KIE value up to 5.16. To further confirm the KIE effect, the pre-synthesized $Ir-D_xWO_3$ (see Methods) also manifests a similar induction period in 1.0 M PBS (H_2O) electrolyte, showing enhanced HER activity (Supplementary Fig. 27). The same process was carried out for Pt/C in Supplementary Fig. 28 for comparison. Pt/C only exhibits the typical isotope effect (KIE = 3.79 at $-0.1 V_{RHE}$) and does not have the above-mentioned induction period phenomenon. Compared with Pt/C, the large KIE value variations of $Ir-H_xWO_3$ ($2.57_{initial} < 3.79_{Pt/C} < 5.16_{final}$) indicate the unsubstitutable role of lattice-hydrogen species in the HER process. Combining operando Raman measurements, selective poisoning and kinetic isotope effect experiments, it unambiguously unveiled that a potential neutral HER mechanism involved lattice WO-H species and metallic Ir site synergistic catalysis pathway in $Ir-H_xWO_3$.

Density functional theory (DFT) calculations were then performed to probe the specific reaction pathway of $Ir-H_xWO_3$. Based on the above catalyst characterization, the computational model adopt Ir_{10} cluster supported on WO_3 (002) with terminal oxygen saturated with

hydrogen atoms to form experimentally validated WO-H species. The possible HER pathway assisted by support-derived lattice-hydrogen species (WO-H) is systematically investigated in comparison to the traditional HER process (Fig. 7a). The adsorption and dissociation of the H_2O molecule were first examined. The absorbed free energy of H_2O at different Ir sites (Ir_1 , Ir_2 , and Ir_3 correspond to the interfacial Ir, subinterfacial Ir and bulk Ir, respectively) are calculated (Supplementary Fig. 29). Clearly, Ir_3 active site is found to be the most favorable (or dominant) site for H_2O adsorption with more negative $\Delta G_{H_2O^*}$ (-0.16 eV) as compared with that of Ir_1 (0.29 eV) and Ir_2 (0.12 eV). Subsequently, $*H_2O$ dissociation is exothermic by 0.66 eV, and the formed H atom is adsorbed on the neighboring Ir_2 site. The Tafel slope for $Ir-H_xWO_3$ suggests that hydrogen evolution over this material should occur via recombination of two H atoms. Then, two Tafel pathways are considered: (1) Traditional Tafel pathway (green line). Another H_2O is adsorbed on Ir_3 and cleaved to $*H$ and hydroxyl; two H atoms on Ir_2 site are preferentially coupled together by Tafel reaction with a high free energy barrier (0.85 eV). (2) Interfacial Tafel pathway involved lattice-hydrogen (violet line). $*H$ on the Ir_2 site undergoes two-steps hydrogen transfer to the Ir_1 site with a substantially low energy barriers (0.41 eV), subsequent Tafel step for Ir_1-*H and adjacent WO- $*H$ species experiences an exothermic process (-0.08 eV), which contributes to fast hydrogen production rate, as obtained experimentally. Moreover, this unique and dominant interfacial dehydrogenation site is further corroborated by H_2 -TPD experiments in Supplementary Fig. 30.

Based on the conclusions obtained from the above experimental and theoretical studies, we propose a possible interfacial hydrogen-evolution pathway mediated by lattice hydrogen of neutral HER catalyzed by hybridized $Ir-H_xWO_3$ (Fig. 7b). The Ir metal component in the hybridized $Ir-H_xWO_3$ possesses superior electrocatalytic activity toward the Volmer process and is expediently utilized to strongly

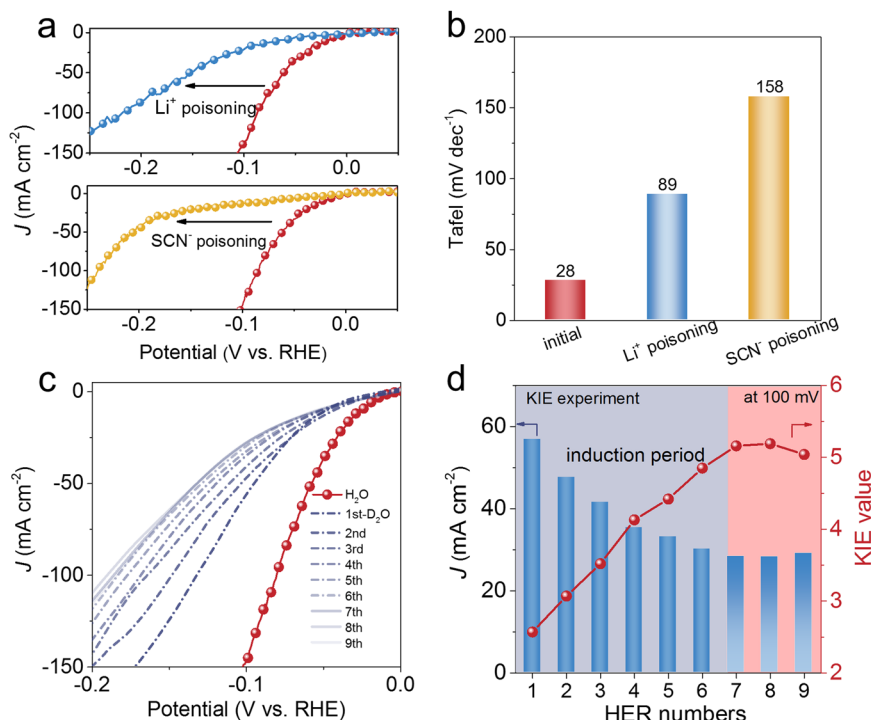


Fig. 6 | Poisoning and KIE experiments. **a** The LSV curves of Ir- H_xWO_3 before and after poisoning metallic Ir sites and WO-H sites, respectively. **b** The Tafel slope comparisons of Ir- H_xWO_3 before and after poisoning experiments. **c** The LSV

curves of Ir- H_xWO_3 in 1.0 M PBS (H_2O and D_2O) electrolyte. **d** Calculated KIE values (J_{H_2O}/J_{D_2O}) under 100 mV overpotential. All electrochemical data were corrected for 95% iR drop.

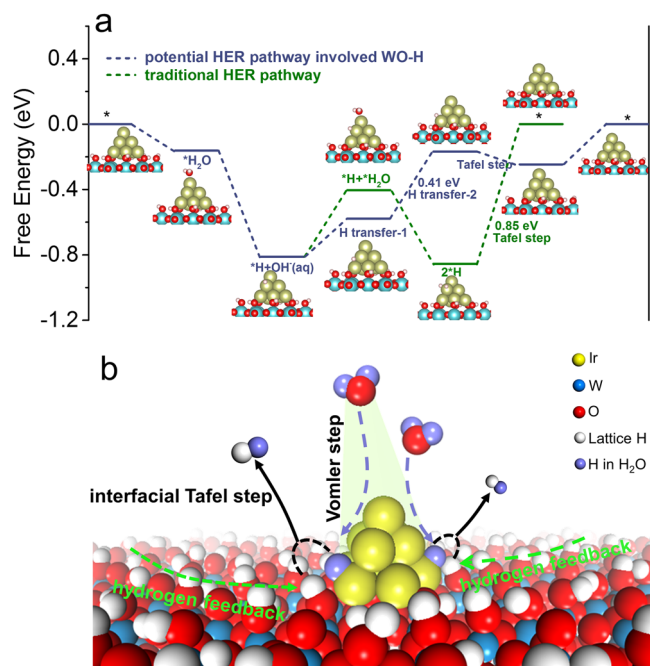


Fig. 7 | DFT calculations and catalytic mechanisms. **a** Free energy profiles for HER over Ir₁₀- H_xWO_3 via different reaction pathways. **b** Schematic illustrating the proposed reaction mechanism on Ir- H_xWO_3 .

adsorb H_2O , effectively catalyze the dissociation of H_2O^* to generate interfacial Ir- H^* . The thermodynamically favorable Tafel process is advantageously utilized to efficiently combine the interfacial Ir- H^* and neighboring reactive WO-H * into H_2 . The hydrogen-deficient state at the interface can be eliminated by the hydrogen transfer on the surface

of H_xWO_3 to replenish hydrogen, thereby realizing the closed loop of the entire catalytic reaction. Additionally, Supplementary Movies 4 and 5 visually demonstrate the continuous replenishment of hydrogen on Ir- H_xWO_3 surface after removing bias, along with Pt/C for comparison. Hence, the exceptional neutral HER electrocatalytic performance of Ir- H_xWO_3 stems from the coherent synergism of Ir and in situ formed lattice-hydrogen components. Inspired by the local acid-like microenvironment created by H_xWO_3 , it is expected to extend “proton sponge” effect of H_xWO_3 support to other $M-H_xWO_3$ systems ($M = Pt, Ru, Pd, Co, Ni$). As expected in Supplementary Fig. 31, compared with conventional M -Carbon catalysts, the significantly reduced overpotentials and accelerated reaction kinetics on $M-H_xWO_3$ systems ($M = Ru, Pt, Pd, Co, Ni$) confirm that the local acid-like microenvironment provided by H_xWO_3 fundamentally enhances the intrinsic HER activity of catalysts in thermodynamically unfavorable neutral media.

Neutral water electrolysis device performance

To highlight the practical significance of localized acidification environmental engineering for neutral water reduction, we further integrated bifunctional Ir- H_xWO_3 catalysts into a membrane electrode assembly (MEA) as cathode and anode materials and assembled an actual anion-exchange-membrane water electrolysis device (Fig. 8a). The current density of the MEA composed of Ir- H_xWO_3 /CFP(±) is much higher than that of the MEA composed of benchmark commercial (-)Pt/C + Ir/C(+) under the same cell voltage. At a current density of 10 mA cm⁻², the cell voltage is 1.78 V for Ir- H_xWO_3 /CFP(±)-based MEA system, which is much less than that of 2.05 V for benchmark commercial (-)Pt/C + Ir/C(+)-based MEA setup (Fig. 8b). Significantly, the Ir- H_xWO_3 /CFP(±) MEA can be stably operated for at least 40 h at a larger current density of 150 mA cm⁻² (Fig. 8c), demonstrating unprecedented application prospects.

In summary, we have developed a facile electrochemical method to synthesize a highly unique Ir- H_xWO_3 catalyst for efficient water splitting in challenging neutral media. The intentionally created local

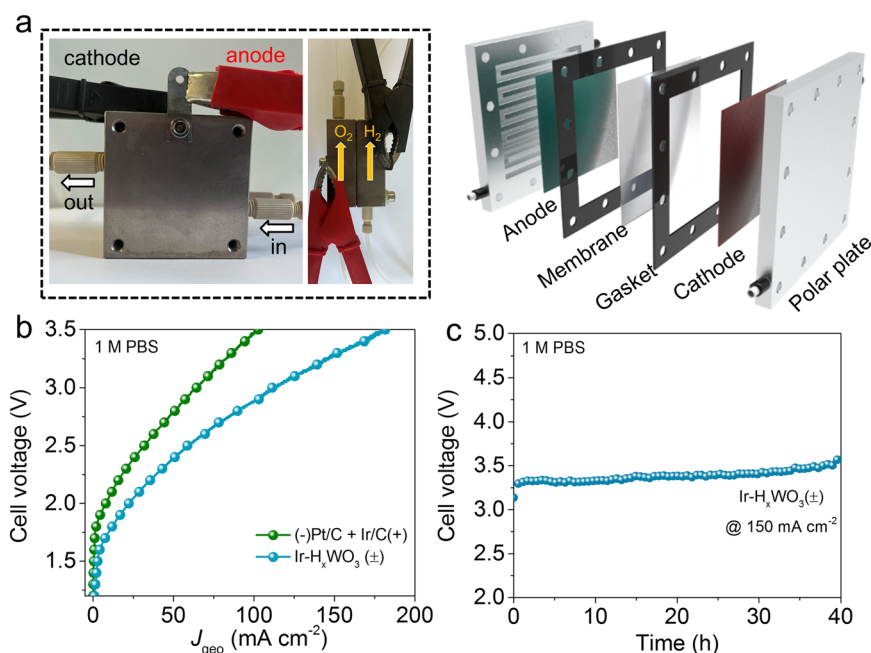


Fig. 8 | Neutral water electrolysis device performance. **a** Photographs and schematic illustration of membrane electrode assembly (MEA) electrochemical reactor, the geometric area of the electrode is 4 cm². **b** Neutral water splitting

performance of the commercial (-)Pt/C + Ir/C(+) and Ir-H_xWO₃/CFP(±) MEA setups at room temperature without iR compensation. **c** Stability tests of the Ir-H_xWO₃/CFP(±) MEA.

acid-like microenvironment around Ir by spontaneous insertion of protons into WO₃ was profoundly verified by the electrochromic process and corresponding physicochemical characterizations. Operando Raman measurements, selective poisoning and kinetic isotope effect experiments confirm the coherent synergism between Ir and lattice-hydrogen species of H_xWO₃, that is, the Volmer process is drastically boosted at Ir site to form Ir-H*, followed by spontaneous recombination of Ir-H* and neighboring revitalized WO-H* species to form H₂ molecular via interfacial Tafel step, as verified by theoretical calculations, thereby keeping the reaction at a high rate. Consequently, the Ir-H_xWO₃ catalyst breaks the traditional pH-dependent kinetics limitations compared with conventional Ir/C and Pt/C systems, showing a low overpotential of 20 mV at 10 mA cm⁻² and Tafel slope of 28 mV dec⁻¹ in neutral media, closing to those in acidic media. A neutral water electrolysis device assembled with Ir-H_xWO₃(±) realizes a cell voltage of 1.78 V at a current density of 10 mA cm⁻² and a high durability of 40 h at a larger current density of 150 mA cm⁻². Therefore, our study provides insight into tailoring the local reaction environment to design high-performance catalysts in a more rational and precise way.

Methods

Chemicals

Iridium(III) chloride hydrate (IrCl₃·xH₂O, 298.58), Ammonium metatungstate ((NH₄)₆H₂W₁₂O₄₀, 2974.32), Ruodium(III) chloride hydrate (RuCl₃·xH₂O, 207.43), Palladium(II) chloride (PdCl₂, 177.32), Chloroplatinic acid hexahydrate (H₂PtCl₆·6H₂O, 517.91), Nickel nitrate hexahydrate (Ni(NO₃)₂·6H₂O, 290.78), Cobalt nitrate hexahydrate (Co(NO₃)₂·6H₂O, 291.03) and Citric acid (C₆H₈O₇, 192.13) were purchased from Aladdin Inc. Commercial 20 wt% Pt/C, 10 wt% Ir/C, 5 wt% Ru/C and 5 wt% Pd/C were purchased from Sigma-Aldrich. The commercial carbon fiber paper (CFP) was purchased from Shanghai Hesen Electric Co.

Synthesis of WO₃

Typically, the WO₃ grown on CFP was prepared by traditional hydrothermal processes followed by heating treatment. The details are as

follows: 0.89 g ammonium metatungstate and 0.18 g citric acid were dissolved in 35 mL deionized water and stirred to form a clear solution. A piece of carbon fiber paper (CFP, approximately 2 cm × 4 cm × 0.2 mm) was carefully cleaned with concentrated HNO₃ solution in an ultrasound bath for several minutes. Then, the CFP was cleaned successively by deionized water, acetone, and absolute ethanol. After the cleaning, the CFP was dried at 60 °C for 30 min. Then, it and the aqueous reagent solution were placed together in a 50 mL Teflon-lined stainless-steel autoclave, which was sealed and maintained at 180 °C for 12 h. The as-synthesized material was then taken out, ultrasonically cleaned for 2 min in deionized water, and dried under vacuum at 70 °C overnight. Finally, the collected sample was placed in muffle furnace and heated to 500 °C at a heating rate of 5 °C min⁻¹ and held for 4 h to obtain WO₃ sample.

Synthesis of Ir-H_xWO₃

Ir-H_xWO₃ was synthesized by a potential-cycling method, which was performed using a CHI 760E electrochemical workstation (Shanghai CHI Instruments Company) and a standard three-electrode cell. 1 M PBS (50 mL) contained 0.2 g L⁻¹ iridium chloride was taken as electrolyte solution. WO₃ precursor, a graphite rod and a saturated calomel electrode (SCE) were used as the working electrode (WE), counter electrode (CE) and reference electrode (RE), respectively. On the WE and CE, different potential cycles (100, 200, 300, 400, 500, and 1000) can be carried out between -0.35 and 0 V vs RHE at a scan rate of 100 mV s⁻¹. We have found that 500 cycles can convert the precursor sample to Ir-H_xWO₃.

Synthesis of M-H_xWO₃ (M = Pt, Ru, Pd, Ni, and Co)

M-H_xWO₃ (M = Ru, Pt, and Pd) were synthesized by the same approach as the preparation of Ir-H_xWO₃, except that metal precursor was changed to ruodium chloride, chloroplatinic acid or palladium chloride, respectively. Commercial 20 wt% Pt/C, 5 wt% Ru/C and 5 wt% Pd/C were used as comparison samples. M-H_xWO₃ (M = Ni and Co) were prepared as following steps. 400 μL 20 g L⁻¹ nickel nitrate or cobalt nitrate was dropped onto 1 × 1 WO₃/CFP, and then dried up. The resulting material was reduced in tube furnace at 500 °C for 3 h in H₂

atmosphere (flow rate: 50 sccm). The same approach was conducted on pure CFP to obtain Ni and Co comparison samples.

Synthesis of H_xWO_3

H_xWO_3 was synthesized by the same approach as the preparation of Ir- H_xWO_3 , except that the pure 1.0 M PBS was taken as electrolyte solution.

Synthesis of Ir- D_xWO_3

Ir- D_xWO_3 was synthesized by the same approach as the preparation of Ir- H_xWO_3 , except that the 1.0 M PBS (D_2O) contained 0.2 g L^{-1} iridium chloride was taken as electrolyte solution.

Characterization

Powder X-ray diffraction (XRD) was performed on a Bruker D8 Advance diffractometer (Cu $K\alpha$, $\lambda = 1.5418\text{ \AA}$) at the operating voltage of at 40 kV and current of 40 mA. TEM and SEM images were taken on a Hitachi-7700 microscope and Hitachi S-4800 microscope, respectively. A JEOL JEM-2100F with a 200 kV acceleration voltage was used to characterize the HRTEM and HAADF-STEM. Electron paramagnetic resonance (EPR) measurements were performed on a Bruker A300 EPR spectrometer. The UV-Vis diffuse reflectance spectra of the samples were obtained by the UV-3600 spectrophotometer in the region of 200–800 nm, with the $BaSO_4$ powder as background. 1H solid-state nuclear magnetic resonance (NMR) measurements were performed at room temperature on a Bruker 400 MHz NMR spectrometer. The content of noble metals in the samples was determined by a Thermo IRIS Intrepid II inductively coupled plasma-optical emission spectrometry (ICP-OES). X-ray photoemission spectra (XPS) were obtained on an Escalab 250XI spectrometer with a monochromatized Al $K\alpha$ source (1486.6 eV) and a base pressure in the lower 2×10^{-7} mbar range, and XPS spectra were calibrated with the C 1s peak at 284.8 eV. High-resolution XPS spectra were acquired with an analyzer pass energy of 40 eV. The XPS spectra were fitted after subtraction of a Shirley background with the available XPSPEAK 4.1 software.

Temperature-programmed desorption-mass spectroscopy (TPD-MS) measurement

In the experiment to investigate the effect of Ir on hydrogen species in H_xWO_3 support, 100 mg of catalyst sample with grain sizes of 60–80 mesh was loaded in a quartz reactor and pretreated with an ultra-pure Ar gas (with a flow rate of 30 ml min^{-1}) at $200\text{ }^\circ\text{C}$ for 2 h to remove the surface-adsorbed species. The pretreated sample was then cooled to room temperature, following which the sample was heated to $800\text{ }^\circ\text{C}$ under the Ar gas flow (30 ml min^{-1}) at a heating rate of $2\text{ }^\circ\text{C min}^{-1}$.

In the experiments to investigate hydrogen desorption sites, after Ar pretreatment, H_2 adsorption was carried in H_2 gas flow (30 ml min^{-1}) for 1 h, followed by purging with Ar gas (30 ml min^{-1}) for 1 h to remove the physically adsorbed H_2 on the sample surface. Finally, a programmed temperature desorption test under Ar gas flow was performed.

The identification of species desorbed during the thermal process was done by re-analyzing the total ion spectra for the specific mass. The main desorbed specie detected is H_2 with $m/e = 2$.

Electrochemical measurements

All electrochemical measurements were performed on a CHI 760E electrochemical workstation (Shanghai CHI Instruments Company) at room temperature. A graphite rod and a saturated calomel electrode were used as the counter electrode and the reference electrode, respectively. The calibration procedure for the reference electrode (SCE) was presented in Supplementary Fig. 32. Ir- H_xWO_3 Samples were cut into $1 \times 1\text{ cm}^2$ and directly used as the working electrode. For commercial Pt/C, Ir/C, Ru/C and Pd/C electrodes, 10.0 mg catalyst powder and 25 μL Nafion solution (5 wt%) were

dispersed in 1.0 ml ethanol solution by sonication for 30 min to get a homogeneous ink. Then, certain amounts of the ink were loaded on a CFP ($1 \times 1\text{ cm}^2$) and dried under infrared lamp. In Fig. 4, Pt or Ir metal loading was $0.1\text{ mg}_{\text{metal}}\text{ cm}^{-2}$ to obtain appreciable catalytic activity. In the activity evaluation of M - H_xWO_3 systems, for parallel comparison, the loading amount of Ru/C, Pt/C and Pd/C comparison samples on CFP was $58\text{ }\mu\text{g}_{\text{Ru}}\text{ cm}^{-2}$, $50\text{ }\mu\text{g}_{\text{Pt}}\text{ cm}^{-2}$ and $65\text{ }\mu\text{g}_{\text{Pd}}\text{ cm}^{-2}$, respectively. All potentials measured were calibrated vs RHE using the following equation: $E(\text{RHE}) = E(\text{SCE}) + 0.244\text{ V} + 0.0592 \times \text{pH}$. For each HER experiment, cathodic linear sweep voltammetry (LSV) was performed in high-purity H_2 -saturated 1.0 M PBS ($\text{pH} = 7.03 \pm 0.08$) or 0.5 M H_2SO_4 ($\text{pH} = 0.35 \pm 0.04$) at a scan rate of 2 mV s^{-1} (the pH value was determined by pH meter, see Supplementary Fig. 33). All the polarization curves were the steady ones after several scans with iR compensation. The iR compensation was adopted by on-the-fly correction with positive feedback mode, where the points were automatically corrected by instruments with built-in iR compensation. A factor of 95% was applied to measure the resistance value of electrolyte at the open circuit potential. Solution resistances in 1.0 M PBS were 0.4 ± 0.1 , 0.6 ± 0.2 , 0.8 ± 0.1 , 1.1 ± 0.2 , and 0.5 ± 0.2 ohm for commercial Pt/C, Ir/C, Ru/C, Pd/C and M - H_xWO_3 samples ($M = \text{Ir, Pt, Ru, Pd, Co, Ni}$), respectively. Solution resistances in 0.5 M H_2SO_4 were 0.3 ± 0.1 , 0.5 ± 0.2 , and 0.3 ± 0.1 ohm for commercial Pt/C, Ir/C and Ir- H_xWO_3 catalysts, respectively. The current density was calculated against the geometric area (1 cm^2) of the electrode to obtain the specific activity. Electrochemical impedance spectroscopy (EIS) measurements were performed from 10^{-2} to 10^5 Hz with an amplitude of 5 mV at an overpotential of 30 mV in 1.0 M PBS solution. The stability measurements were performed by transient accelerating degradation technique (ADT) protocol and static chronopotentiometry test in 1.0 M PBS solution. ADT tests were conducted as follows. Typically, square-wave voltammetry consisting of 10,000 cycles were conducted between a higher potential of $0.15\text{ V}_{\text{RHE}}$ and a lower potential of $-0.35\text{ V}_{\text{RHE}}$. Each cycle was maintained for 4 s. Chronopotentiometry was measured at 10 and 500 mA cm^{-2} to represent typical static long-term stability tests.

Measurement of pH on the catalyst surface

According to previous work⁴⁴, the pH values on the catalyst surfaces were measured by the rotating ring-disk electrode (RRDE) technique. The potential of Pt ring electrode (RE, 0.1866 cm^2) is sensitive to pH and can be used to monitor the variations in the pH on the disk electrode (DE, 0.2475 cm^2) surface. A three-electrode cell was constructed of the RRDE, graphite rod and a saturated calomel electrode (SCE) as working, counter, and reference electrodes, respectively. Then, the pH dependence of the open circuit potential (E_{ocp}) in H_2 -saturated 1.0 M PBS solution was measured with Pt RE (Supplementary Fig. 5). The OCP of the Pt electrode would indicate the equilibrium potential of $2H^+ + 2e^- \rightarrow H_2$, which varies with pH according to the Nernst equation:

$$E(\text{V vs. SHE}) = \frac{-2.303RT}{F} \text{pH} \quad (3)$$

The fugacity of H_2 is assumed to be equal to unity and R , T , and F are the gas constant, the absolute temperature, and the Faraday constant.

For measuring the pH on the electrode surface, the investigated catalyst was loaded onto the disk electrode. The catalyst ink was prepared by ultrasonically dispersing catalyst powder (5 mg) in 5 wt% Nafion solution (20 μL) and ethanol (480 μL) mixed solution. 10 μL of catalyst ink (10.0 mg mL^{-1}) was then transferred onto the disk electrode (catalyst loading: 0.4 mg cm^{-2}). The pH measurements on the catalyst surfaces were conducted in 1.0 M PBS solution with the working electrode rotating at a speed of 1600 rpm. Constant potential method was performed on the disk electrode ($E = 0.1, 0, -0.1, -0.2, -0.3, -0.4, -0.5, -0.6, \text{ and } -0.7\text{ V}_{\text{RHE}}$ for 200 s) to obtain a steady-state

current response (j), and OCP was simultaneously measured on the Pt ring electrode. The pH value of the catalyst-loaded DE can be deduced from the pH value of the Pt RE by the following equation:

$$c_{\text{rt,H}^+} - c_{\text{rt,OH}^-} = N_{\text{D}}(c_{\text{d,H}^+} - c_{\text{d,OH}^-}) + (1 - N_{\text{D}})(c_{\infty,\text{H}^+} - c_{\infty,\text{OH}^-}) \quad (4)$$

where $c_{\text{rt,H}^+}$ and $c_{\text{d,H}^+}$ are the concentrations of H^+ on the RE and DE, respectively, $c_{\text{rt,OH}^-}$ and $c_{\text{d,OH}^-}$ are the concentrations of OH^- on the RE and DE, respectively, c_{∞,H^+} and c_{∞,OH^-} are the concentrations of H^+ and OH^- in the bulk electrolyte, respectively, and $N_{\text{D}} = 0.37$ is the collection efficiency of the RE.

Neutral water electrolysis device

For a neutral water electrolysis device system, the bifunctional Ir- $\text{H}_x\text{WO}_3/\text{CP}$ catalysts ($2 \times 2 \text{ cm}^2$) were both for the anodic OER and cathodic HER. As for benchmark commercial (-)Pt/C + Ir/C(+) partners, homogeneous slurries consisting of catalysts, Nafion solution (5.0 wt.%) and ethanol were air-sprayed onto the carbon fiber paper with an iridium black loading of 2.0 mg cm^{-2} for the anode and 1.0 mg cm^{-2} of Pt/C for the cathode. In all, 1.0 M PBS electrolyte was cycled both on the anodic and cathodic sides by a peristaltic pump, and the flow rate is 80 mL min^{-1} . Anion-exchange membrane (Fumasep FAA-3-PK-130) was used to isolate the cathode and anode. Polarization curves were collected from 1.0 to 3.5 V at room temperature under ambient pressure. The current density was calculated against the geometric area (4 cm^2) of the MEA to obtain the specific activity without iR compensation. The stability test was carried out by galvanostatic electrolysis at a constant current density of 150 mA cm^{-2} .

Operando Raman spectroscopy measurement

Operando Raman spectra were recorded on a LabRAMHR Evolution with an Ar⁺ laser of 514 nm excitation under controlled potentials by the electrochemical workstation. The electrolytic cell was homemade by Teflon with thin round quartz glass plate as cover to protect the objective. The Ir- H_xWO_3 and H_xWO_3 were directly used as working electrode. The Ag/AgCl electrode with inner reference electrolyte of 1.0 M KCl and a Pt wire serves as the reference electrode and the counter electrode, respectively. 1.0 M PBS was used as electrolyte and chronoamperometry measurements were conducted at the potential range from 0 to $-0.30 \text{ V}_{\text{RHE}}$ with the interval of 50 mV. The spectrum was obtained from at least 20 points to ensure accuracy of the information about the samples. The applied voltage–time of each point is 100 s, and the Raman test began when the time exceeded 60 s.

Computational section

The Density Functional Theory (DFT) calculations were performed in the Vienna Ab initio simulation package (VASP) with the Perdew-Burke-Emzerhof (PBE). The projector augmented wave (PAW) functional was selected as the generalized gradient approximation (GGA) to describe the electron-ion interactions. The cut-off energy of 400 eV and Gaussian electron smearing method with $\sigma = 0.05 \text{ eV}$ were used. A vacuum of 15 \AA was adopted along the z-axis. And $(5 \times 5 \times 1)$ and $(2 \times 2 \times 1)$ Monkhoest-Pack k-point mesh were used for all samples during electronic structure calculation and the structure optimization, respectively. During structure optimization, the geometry optimization was performed when the convergence criterion on forces became smaller than 0.02 eV \AA^{-1} and the energy difference was $<10^{-4} \text{ eV}$. To model the Ir- H_xWO_3 catalyst, the Ir₁₀ clusters were supported on 4×4 supercells of WO_3 (002) with surface O atoms saturated with H atoms. The atoms in the bottom two layers of WO_3 (002) were kept frozen while the remaining were allowed to relax during the slab calculations. Gibbs free energy of X species ($X = \text{H}_2\text{O}$ and H) adsorption is calculated by

$$\Delta G = \Delta E_{\text{X}/\text{surf}} - \Delta E_{\text{surf}} - uE_{\text{X}} + \Delta E_{\text{ZPE}} - T\Delta S_{\text{H}} \quad (5)$$

where $E_{\text{X}/\text{surf}}$ is the total energy of the surface with adsorbate, E_{surf} is the energy of the clean surface, E_{X} is the energy of adsorbate, ΔE_{ZPE} represents the zero-point energy of the system, and $T\Delta S_{\text{H}}$ is the contribution from entropy.

Data availability

The authors declare that all data supporting the findings of this study can be found in the manuscript and Supplementary Information, or are available from the corresponding authors upon request.

References

- Dresselhaus, M. S. & Thomas, I. L. Alternative energy technologies. *Nature* **414**, 332–337 (2001).
- Turner, J. A. Sustainable hydrogen production. *Science* **305**, 972–974 (2004).
- Zheng, X. et al. In situ formed bimetallic carbide Ni₆Mo₆C nanodots and NiMoO_x nanosheet array hybrids anchored on carbon cloth: efficient and flexible self-supported catalysts for hydrogen evolution. *ACS Catal.* **10**, 11634–11642 (2020).
- Wang, P. et al. Interface engineering of Ni_xS_y@ MnO_xH_y nanorods to efficiently enhance overall-water-splitting activity and stability. *Nano-Micro Lett.* **14**, 120 (2022).
- Xu, X., Sun, H., Jiang, S. P. & Shao, Z. Modulating metal-organic frameworks for catalyzing acidic oxygen evolution for proton exchange membrane water electrolysis. *SusMat* **1**, 460–481 (2021).
- Ali, A., Long, F. & Shen, P. K. Innovative strategies for overall water splitting using nanostructured transition metal electrocatalysts. *Electrochem. Energy Rev.* **5**, 1 (2022).
- Wang, P. et al. MnO_x-decorated nickel-iron phosphides nanosheets: interface modifications for robust overall water splitting at ultra-high current densities. *Small* **18**, e2105803 (2022).
- Resasco, J. et al. Enhancing the connection between computation and experiments in electrocatalysis. *Nat. Catal.* **5**, 374–381 (2022).
- Chatenet, M. et al. Water electrolysis: from textbook knowledge to the latest scientific strategies and industrial developments. *Chem. Soc. Rev.* **51**, 4583–4762 (2022).
- Zhu, J., Hu, L., Zhao, P., Lee, L. Y. S. & Wong, K. Y. Recent advances in electrocatalytic hydrogen evolution using nanoparticles. *Chem. Rev.* **120**, 851–918 (2020).
- Li, J., Stenlid, J. H., Ludwig, T., Lamoureux, P. S. & Abild-Pedersen, F. Modeling potential-dependent electrochemical activation barriers: revisiting the alkaline hydrogen evolution reaction. *J. Am. Chem. Soc.* **143**, 19341–19355 (2021).
- Wang, X. et al. Strategies for design of electrocatalysts for hydrogen evolution under alkaline conditions. *Mater. Today* **36**, 125–138 (2020).
- Dai, J. et al. Hydrogen spillover in complex oxide multifunctional sites improves acidic hydrogen evolution electrocatalysis. *Nat. Commun.* **13**, 1189 (2022).
- Subbaraman, R. et al. Enhancing hydrogen evolution activity in water splitting by tailoring Li⁺-Ni(OH)₂-Pt interfaces. *Science* **334**, 1256–1260 (2011).
- Tan, H. et al. Engineering a local acid-like environment in alkaline medium for efficient hydrogen evolution reaction. *Nat. Commun.* **13**, 2024 (2022).
- Wang, X., Xu, C., Jaroniec, M., Zheng, Y. & Qiao, S. Z. Anomalous hydrogen evolution behavior in high-pH environment induced by locally generated hydronium ions. *Nat. Commun.* **10**, 4876 (2019).
- Jin, H. et al. Stable and highly efficient hydrogen evolution from seawater enabled by an unsaturated nickel surface nitride. *Adv. Mater.* **33**, 2007508 (2021).
- Wang, J. et al. Heteroatom-doping of non-noble metal-based catalysts for electrocatalytic hydrogen evolution: an electronic structure tuning strategy. *Small Methods* **5**, e2000988 (2021).

19. Guo, J. et al. Direct seawater electrolysis by adjusting the local reaction environment of a catalyst. *Nat. Energy* **8**, 264–272 (2023).
20. Stamenkovic, V. et al. Energy and fuels from electrochemical interfaces. *Nat. Mater.* **16**, 57–69 (2017).
21. Dinh, C. T. et al. Multi-site electrocatalysts for hydrogen evolution in neutral media by destabilization of water molecules. *Nat. Energy* **4**, 107–114 (2018).
22. Zhai, L. et al. Modulating built-in electric field via variable oxygen affinity for robust hydrogen evolution reaction in neutral media. *Angew. Chem. Int. Ed.* **61**, e202116057 (2022).
23. Deng, L. et al. Electronic modulation caused by interfacial Ni-O-M (M = Ru, Ir, Pd) bonding for accelerating hydrogen evolution kinetics. *Angew. Chem., Int. Ed.* **60**, 22276–22282 (2021).
24. Lu, K. et al. Li_xNiO/Ni heterostructure with strong basic lattice oxygen enables electrocatalytic hydrogen evolution with Pt-like activity. *J. Am. Chem. Soc.* **142**, 12613–12619 (2020).
25. Maiti, S. et al. Engineering electrocatalyst nanosurfaces to enrich the activity by inducing lattice strain. *Energy Environ. Sci.* **14**, 3717–3756 (2021).
26. Zheng, X. et al. Strong oxide-support interaction over IrO₂/V₂O₅ for efficient pH-universal water splitting. *Adv. Sci.* **9**, e2104636 (2022).
27. Kim, T. et al. Highly dispersed Pt clusters on F-doped tin(IV) oxide aerogel matrix: an ultra-robust hybrid catalyst for enhanced hydrogen evolution. *ACS Nano* **16**, 1625–1638 (2022).
28. Yuan, L.-P., Tang, T., Hu, J.-S. & Wan, L.-J. Confinement strategies for precise synthesis of efficient electrocatalysts from the macroscopic to the atomic level. *Acc. Mater. Res.* **2**, 907–919 (2021).
29. Billeter, E. et al. Hydrogen in tungsten trioxide by membrane photoemission and density functional theory modeling. *Phys. Rev. B* **103**, 205304 (2021).
30. Vanags, M. et al. Membrane-less amphoteric decoupled water electrolysis using WO₃ and Ni(OH)₂ auxiliary electrodes. *Energy Environ. Sci.* **15**, 2021–2028 (2022).
31. Zhu, H. et al. Direct electrochemical protonation of metal oxide particles. *J. Am. Chem. Soc.* **143**, 9236–9243 (2021).
32. Bian, Z., Zhao, J., Cao, H., Dong, Y. & Luo, Z. Reversible rapid hydrogen doping of WO₃ in non-acid solution. *ACS Appl. Mater. Interfaces* **13**, 13419–13424 (2021).
33. Miu, E. V. & McKone, J. R. Comparisons of WO₃ reduction to H_xWO₃ under thermochemical and electrochemical control. *J. Mater. Chem. A* **7**, 23756–23761 (2019).
34. Li, Y. F. et al. Cu atoms on nanowire Pd/H_yWO_{3-x} bronzes enhance the solar reverse water gas shift reaction. *J. Am. Chem. Soc.* **141**, 14991–14996 (2019).
35. Pfriem, N. et al. Impact of the local concentration of hydronium ions at tungstate surfaces for acid-catalyzed alcohol dehydration. *J. Am. Chem. Soc.* **143**, 20133–20143 (2021).
36. Fu, J. et al. Modulating the dynamics of Brønsted acid sites on PtWO_x inverse catalyst. *Nat. Catal.* **5**, 144–153 (2022).
37. Tian, H. et al. Oxygen vacancy-assisted hydrogen evolution reaction of the Pt/WO₃ electrocatalyst. *J. Mater. Chem. A* **7**, 6285–6293 (2019).
38. Peng, C., Zhao, W., Kuang, Z., Miller, J. T. & Chen, H. Boosting neutral hydrogen evolution reaction on iridium by support effect of W₁₈O₄₉. *Appl. Catal. A: Gen.* **623**, 118293 (2021).
39. Zhang, W. et al. WO_x-surface decorated PtNi@Pt dendritic nanowires as efficient pH-universal hydrogen evolution electrocatalysts. *Adv. Energy Mater.* **11**, 2003192 (2020).
40. Park, J. et al. Investigation of the support effect in atomically dispersed Pt on WO_{3-x} for utilization of Pt in the hydrogen evolution reaction. *Angew. Chem. Int. Ed.* **58**, 16038–16042 (2019).
41. Wang, G. et al. Hydrogen-treated WO₃ nanoflakes show enhanced photostability. *Energy Environ. Sci.* **5**, 6180 (2012).
42. Vivier, V. & Orazem, M. E. Impedance analysis of electrochemical systems. *Chem. Rev.* **122**, 11131–11116 (2022).
43. Sellers, M. C. K. & Seebauer, E. G. Measurement method for carrier concentration in TiO₂ via the Mott-Schottky approach. *Thin Solid Films* **519**, 2103–2110 (2011).
44. Yokoyama, Y., Miyazaki, K., Miyahara, Y., Fukutsuka, T. & Abe, T. In situ measurement of local pH at working electrodes in neutral pH solutions by the rotating ring-disk electrode technique. *Chem-ElectroChem* **6**, 4750–4756 (2019).
45. Yokoyama, Y. et al. In situ local pH measurements with hydrated iridium oxide ring electrodes in neutral pH aqueous solutions. *Chem. Lett.* **49**, 195–198 (2020).
46. Miu, E. V., McKone, J. R. & Mpourmpakis, G. The sensitivity of metal oxide electrocatalysis to bulk hydrogen intercalation: hydrogen evolution on tungsten oxide. *J. Am. Chem. Soc.* **144**, 6420–6433 (2022).
47. Ning, S. et al. Anomalous defect dependence of thermal conductivity in epitaxial WO₃ thin films. *Adv. Mater.* **31**, 903738 (2019).
48. Zheng, T. et al. Conductive tungsten oxide nanosheets for highly efficient hydrogen evolution. *Nano Lett.* **17**, 7968–7973 (2017).
49. Xu, J. et al. Acidity of mesoporous MoO_x/ZrO₂ and WO_x/ZrO₂ materials: a combined solid-state nmr and theoretical calculation study. *J. Phys. Chem. B* **110**, 10662–10671 (2006).
50. Dvořák, F. et al. Bulk hydroxylation and effective water splitting by highly reduced cerium oxide: the role of O vacancy coordination. *ACS Catal.* **8**, 4354–4363 (2018).
51. Becke, A. D. & Edgecombe, K. E. A simple measure of electron localization in atomic and molecular systems. *J. Chem. Phys.* **92**, 5397–5403 (1990).
52. Zheng, W. iR compensation for electrocatalysis studies: considerations and recommendations. *ACS Energy Lett.* **8**, 1952–1958 (2023).
53. Wang, H., Zhang, L., Wang, K., Sun, X. & Wang, W. Enhanced photocatalytic CO₂ reduction to methane over WO₃·0.33H₂O via Mo doping. *Appl. Catal., B* **243**, 771–779 (2019).
54. Garcia-Sanchez, R. F., Ahmido, T., Casimir, D., Baliga, S. & Misra, P. Thermal effects associated with the Raman spectroscopy of WO₃ gas-sensor materials. *J. Phys. Chem. A* **117**, 13825–13831 (2013).
55. Zhu, J. et al. Intrinsic defects and H doping in WO₃. *Sci. Rep.* **7**, 40882 (2017).
56. Du, Q., Freysz, E. & Shen, Y. R. Vibrational spectra of water molecules at quartz/water interfaces. *Phys. Rev. Lett.* **72**, 238–241 (1994).
57. Zhu, J. S. et al. An In situ Raman study of intermediate adsorption engineering by high-index facet control during the hydrogen evolution reaction. *Inorg. Chem. Front.* **7**, 1892–1899 (2020).
58. Zhao, D. et al. Synergistically interactive pyridinic-N-MoP sites: identified active centers for enhanced hydrogen evolution in alkaline solution. *Angew. Chem. Int. Ed.* **59**, 8982–8990 (2020).
59. Fu, H. Q. et al. Hydrogen spillover-bridged volmer/tafel processes enabling ampere-level current density alkaline hydrogen evolution reaction under low overpotential. *J. Am. Chem. Soc.* **144**, 6028–6039 (2022).

Acknowledgements

Financial support from the National Key R&D Program of China (2021YFB3801600), the “Pioneer” and “Leading Goose” R&D Program of Zhejiang (2023C01108, 2022C01218, and 2022C01151), and the National Natural Science Foundation of China (21872121 and 21908189) are greatly appreciated.

Author contributions

X.Z. carried out most of the experimental work and wrote the manuscript. X.S. assisted the experimental work and discussed the results. X.Z., H.N., and R.Y. performed the DFT calculations. B.L., Q.L., S.M., and L.X. helped to polish the paper and discussed the results. Y.W. conceived the project and directed the overall work and manuscript writing. All the authors reviewed and contributed to this paper.

Competing interests

The authors declare no competing interests.

Additional information

Supplementary information The online version contains supplementary material available at <https://doi.org/10.1038/s41467-023-39963-8>.

Correspondence and requests for materials should be addressed to Yong Wang.

Peer review information *Nature Communications* thanks Prafulla K. Jha and the other anonymous reviewers for their contribution to the peer review of this work. A peer review file is available.

Reprints and permissions information is available at <http://www.nature.com/reprints>

Publisher's note Springer Nature remains neutral with regard to jurisdictional claims in published maps and institutional affiliations.

Open Access This article is licensed under a Creative Commons Attribution 4.0 International License, which permits use, sharing, adaptation, distribution and reproduction in any medium or format, as long as you give appropriate credit to the original author(s) and the source, provide a link to the Creative Commons licence, and indicate if changes were made. The images or other third party material in this article are included in the article's Creative Commons licence, unless indicated otherwise in a credit line to the material. If material is not included in the article's Creative Commons licence and your intended use is not permitted by statutory regulation or exceeds the permitted use, you will need to obtain permission directly from the copyright holder. To view a copy of this licence, visit <http://creativecommons.org/licenses/by/4.0/>.

© The Author(s) 2023